Sigl, K.M., Hardin, R., Stephens, R.I., and Beckermann, C., "Fatigue of 8630 Cast Steel in the Presence of Shrinkage Porosity," in Proceedings of the 57th SFSA Technical and Operating Conference, Paper No. 3.5, Steel Founders' Society of America, Chicago, IL, 2003.

FATIGUE OF 8630 CAST STEEL IN THE PRESENCE OF SHRINKAGE POROSITY

K.M. Sigl[1], R.A. Hardin[2], R.I. Stephens[3], and C. Beckermann[3]

[1]Research Assistant, Mechanical and Industrial Engineering Dept. The University of Iowa
[2]Research Engineer, Mechanical and Industrial Engineering Dept. The University of Iowa
[3]Professor, Mechanical and Industrial Engineering Dept. The University of Iowa

Abstract

Steel specimens were cast having varying amounts of porosity. The specimen castings were designed using a computer model that predicts the location and volume percentages of porosity in castings with a sensitivity not yet offered in commercial software. Four specimen geometries having porosity ranging from micro- to macro-scopic were cast from 8630 steel, and monotonic and fatigue properties were obtained to determine the effect of shrinkage porosity on the mechanical performance of the cast steel. Axial fatigue tests were conducted under fully reversed conditions in both strain and load control on specimens containing microporosity, and in load control for specimens containing macropores. Monotonic tests revealed that specimens containing microporosity had strength properties comparable to sound material, but with substantially reduced ductility (66% less reduction in area). Specimens containing macroporosity performed significantly poorer than specimens that contained microporosity in fatigue testing. At stress amplitudes of 126 MPa, specimens with microporosity were found to have lives greater than 5 million cycles (runout) whereas the specimens with macroporosity had fatigue lives were in the 10^2 to 10^4 cycle range at the same stress level. Fatigue lives for macroporosity specimens were in a range from 10^4 to 10^6 cycles when tested at the lowest stress amplitude, 53 MPa. Measured specimen modulus was found to vary with porosity volume and was shown to have a correlation with the fatigue life, with the higher modulus specimens outperforming the lower modulus specimens. Conventional models of fatigue behavior, the strain-life and linear elastic fracture mechanics (LEFM) approaches, were applied to calculate fatigue lives of the cast steel specimens and determine the validity of applying these models in predicting the performance of this cast steel containing a wide range of porosity. Life calculations made using the strain-life approach gave good agreement with measurements for specimens having microporosity, but this approach gave non-conservative results for macroporosity. The LEFM modeling approach gave non-conservative results for both micro- and macro-porosity specimens. Uncertainties and difficulties in modeling macroporosity were found to be their torturous shape, large size relative to the specimen, and the inability to determine the specific macropores responsible for fatigue failure of the specimens which is necessary for direct model-measurement comparisons.

Introduction

Shrinkage porosity in steel castings is a central concern of foundries. It results if there is insufficient liquid metal to feed a casting section as molten steel contracts during solidification. All porosity is detrimental to strength and fatigue life of cast components because the pores act as stress risers within the casting and cracks can nucleate at pores leading to fracture. Despite this, the quantitative impact of porosity on the fatigue behavior of steel castings is not fully understood, and there are no physics-based approaches to consider effect of porosity on casting performance. As a consequence, design engineers have little choice but to use overly large safety factors in many designs, resulting in over-designed, heavy, and expensive castings leading to increased costs and lead time, while decreasing casting yield and productivity.

Since there are no performance-based guidelines for design of cast components where the amount or location of porosity is considered, it is difficult to assess during the design stage whether a cast component will be produced at a high enough quality level to meet its performance requirements. This is particularly true should microporosity occur within the casting. Conversely, a casting might be designed and specified at too high a quality level resulting in an over designed, over priced part. Current criteria for the acceptance or rejection of steel castings, such as the ASTM standard casting radiographs,[1-3] define only the "qualitative" amount of porosity allowed in a casting. These standards consider only the relative amount of porosity present in the casting and not the location or the size of the porosity contained within the casting and its relationship to the design. Furthermore, the radiographic standards do not address microporosity which may be undetectable, but is known to have a detrimental effect on material properties.

The size and location of porosity has been shown to influence the fatigue strength of various castings with larger pores resulting in shorter fatigue lives.[4-8] During fully reversed plane bending tests of 13 chrome stainless steel castings containing surface discontinuities, it was determined that shrinkage cavities less than 3 mm^2 reduced the fatigue strength at 10^7 cycles of the material by 35% while shrinkage cavities greater than 3 mm^2 had reduction in fatigue strengths up to 50%.[4] In another study, it was observed in cast steel specimens tested under rotating bending that the centerline shrinkage cavity had no effect on fatigue life if the diameter of the cross-section of the shrinkage cavity was smaller than one tenth of the diameter of the specimen[5]. However, if the shrinkage cavity was larger than one tenth of the specimen diameter or the cavity deviated from the center of the specimen, the cavity was found to significantly decrease the fatigue strength and fatigue limit. It is clear that the performance of a casting will depend on size and location of the porosity and the loading conditions.

The primary methods to calculate fatigue lives of cast specimens containing porosity involve modeling pores as equivalent notches or cracks.[4,7,9-12] Modeling of pores as elliptical or semi-elliptical cracks, is the most common technique, but modeling pores as three dimensional ellipsoidal notches has also been evaluated.[9] Modeling pores as three dimensional notches uses the local strain approach to calculate the fatigue lives of components. The local strain model assumes that crack nucleation encompasses the majority of the life of the component and that the life-time for fatigue crack propagation to fracture will be insignificant relative to nucleation. The local strain approach requires that pore geometry information, primarily the minimum notch

radius and the major axes of the ellipsoidal notch, be known or determined from the fracture surfaces of tested specimens to determine a stress concentration factor, K_t.

Linear elastic fracture mechanics, LEFM, is used to model pores as pre-existing cracks within the component, and assumes that crack propagation will consume the majority of the fatigue life. Assuming mode I crack growth, this model requires the calculation of a stress intensity factor, K_I, at the crack tip, which is based on crack geometry, component geometry, and loading conditions. Crack propagation is generally assumed to follow the Paris equation. Failure of the component is commonly taken when the remaining net section area stress of the component is at or greater than the yield strength. Applications of this model were used in references [4, 7, 9, 10].

In this investigation, the effects of porosity resulting from shrinkage cavities on the fatigue behavior of axially loaded 8630 quenched and tempered cast steel specimen were measured. Then some typical methods used to predict fatigue life were used to calculate the fatigue lives of the specimens. In order to produce the test specimens, a new porosity prediction algorithm was used to predict, design and produce cast specimens having a wide range of porosity as shown in Figure 1.[13] This algorithm has been implemented within the commercial casting simulation software MAGMAsoft as a software module.[14] It is capable of predicting porosities from radiographically undetectable microporosity to macroporosity. Four casting geometries were designed with this software to produce three levels of macroporosity specimens (termed “least”, “middle” and “most”), and test specimens with only microporosity. Fatigue testing in accordance with ASTM standards was then performed using 10 stress/strain amplitudes for 14 microporosity specimens, and 4 stress amplitudes for 25 macroporosity specimens. Fractography and microscopy were conducted on the fracture surfaces using a scanning electron microscope, SEM, upon completion of mechanical testing.

Analysis was conducted on both the macro and microscopic levels using specimens from each porosity group to understand the fracture morphology and pore geometry. Regions of fatigue crack nucleation and growth were of particular interest and were studied to determine the actual cause of failure. Determination of the pore sizes, shapes, and locations responsible for specimen failure are required in fatigue life calculations. Microscopy was performed to obtain what could be considered average pore geometries and volumes from ground surfaces from within the gage sections of the specimen groups. This information combined with the crack nucleation data gathered from fractography was used to create a representation of porous specimen fatigue life. Microscopy work was also conducted on sections cut from the microporosity specimens. These examinations agreed with predictions from the new porosity modeling algorithm, which had predicted microporosity within the specimens. This predictive capability is not present in solidification software currently on the market.

Experimental Procedure

Test Specimens

Test specimens used in this investigation were prepared from AISI 8630 quenched and tempered cast steel. Microporosity specimens, shown in Figure 2(a), were cast with reservoirs of

molten steel at the ends of the blank with a narrow gage section located in the center in an attempt to minimize the occurrence of macroshrinkage in the casting. Specimens with macroporosity, Figure 2(b), were cast from 14 mm diameter cylinders with an approximate 25 mm diameter disk located at the mid-length of the casting to create a hot spot where the porosity would form. The amount of shrinkage in the casting was controlled by changing the thickness of the central disk, with more shrinkage porosity occurring in the castings with thicker disks.

All cast blanks received the same heat treatment; normalized at 900° C, austenized at 885° C, water quenched, and finally tempered for one and one half hours at 510° C. This heat treatment resulted in a tempered martensitic structure with Rockwell C hardness of 34. This heat treatment was chosen to be the same process used in an earlier 1982 SFSA report[15] in order to create specimens with similar material properties to this baseline data. The specimens from the 1982 SFSA report were machined from large cast trapezoidal-shaped keel blocks, and data from this study will be referred to as the "sound" specimen data throughout the remainder of this paper. After heat treatment, each cast specimen blank was machined into a round specimen according to ASTM E606[16] standards with the final polished dimensions as shown in Figure 3.

The machined specimens were examined through visual inspection and radiographic analysis to determine a qualitative measure of the porosity present in each casting group. Typical radiographs of selected specimens are shown in Figure 4. Visual inspection showed that 2 of the 15 microporosity specimens and 27 of the 29 specimens with macroporosity had exposed pores at the specimen surface. Based on visual inspection of the radiographs, it was observed that the "least" and "middle" porosity groups contain very similar amounts of porosity, while the "most" porosity group of specimens showed the presence of larger voids. No porosity was detectable in the radiographs of the microporosity specimens, so they appeared to be radiographically sound. The micropores were too small to be detectable by the radiographic analysis used.

Mechanical Testing

Testing was performed using a 100 kN closed loop servo-hydraulic test system. All fatigue tests were performed under fully reversed, R = -1, loading conditions. The alignment of the load frame gripping fixtures was verified according to ASTM Standard Practice E1012, Type A Method 1, and meeting the requirements of ASTM E606, which requires that "the maximum bending strains so determined should not exceed 5% of the minimum axial strain range imposed during any test program."[16, 17]

Monotonic and fatigue property data of the 8630 steel with microporosity were obtained first, before the macroporosity specimens. Monotonic tests were conducted in displacement control following the methods described in ASTM E8.[18] Testing procedures for strain controlled low cycle fatigue (LCF) tests outlined in E 606 were followed to gather the needed cyclic and fatigue properties.[16] Tests conducted in strain control had constant strain rates of 0.01 s^{-1} with frequencies varying between 0.25 and 1.25 Hz. At smaller strain amplitudes, the behavior of the specimens was predominately elastic, making it possible to approximate strain amplitudes using load control. Cycling specimens in load control allowed the testing speed to be increased to 10-30 Hz with lower frequencies used for higher stress amplitudes.

All “least”, “middle”, and “most” macroporosity specimens were run in load control at 10-20 Hz. The extensometer was also used on these tests to produce readings for the elastic modulus, E. These data were collected to determine if a relationship between the apparent elastic modulus and the porosity volume measured from the radiographs could be established. The specimens with macroporosity were run at four different stress levels with the first stress level chosen as 126 MPa; this was the run-out stress amplitude for the specimens with microporosity. The second stress level of 66 MPa was chosen by converting the ε-N curve of the microporosity specimens to a stress-life curve, S-N, and then shifting this curve down to the lives of the specimens with macroporosity previously tested. This adjusted S-N curve was then used to estimate stress amplitude and lives of the specimens with macroporosity. The goal was to obtain a life on the order of 10^6 cycles without a run-out occurring. The remaining stress levels were chosen to fill in gaps within the macroporosity specimen data. All fatigue tests were performed until fracture of the specimen occurred, or a run-out life was achieved at $5x10^6$ cycles.

Experimental Results

Monotonic Testing

Monotonic material properties were obtained from two microporosity specimens with the average results shown in Table 1 compared to those of the sound specimens.[15] Monotonic stress-strain curves for the specimens with microporosity are shown in Figure 5. As is evident in Table 1, both groups of material gave similar properties for Young’s Modulus, E, ultimate tensile strength, S_u, and yield strength, S_y, found by the 0.2% offset method, while the percent reduction of area, %RA, was found to be significantly lower in value (75% lower). Neither monotonic test showed signs of necking, and, in conjunction with small values of %RA, and percent elongation, %EL, indicate that the specimens with microporosity exhibited low ductility.

Microporosity Specimen Fatigue Testing

Cyclic and fatigue material properties for the microporosity specimens are shown Table 2, again compared with the results of the sound specimens.[15] The tests were used to create a cyclic σ-ε curve as well as a strain versus reversals to failure, ε-$2N_f$, curve, shown in Figures 5 and 6, respectively. The ε-$2N_f$ curve of Figure 6 is composed of both plastic and elastic curves, which when summed produce the total ε-$2N_f$ curve equation as shown below:

$$\frac{\Delta\varepsilon}{2} = \frac{\Delta\varepsilon_e}{2} + \frac{\Delta\varepsilon_p}{2} = \frac{\sigma'_f}{E}\left(2N_f\right)^b + \varepsilon'_f\left(2N_f\right)^c \qquad (1)$$

$\Delta\varepsilon/2$ = total strain amplitude
$\Delta\varepsilon_e/2$ = elastic strain amplitude
$\Delta\varepsilon_p/2$ = plastic strain amplitude
σ_f' = fatigue strength coefficient
b = fatigue strength exponent
ε_f'= fatigue ductility coefficient

c = fatigue ductility exponent

where the first addition term is the equation of the elastic strain amplitude curve, and the second term is the equation of the plastic strain amplitude curve. Many steels behave in a predominately plastic manner under high strain amplitudes, and in a predominately elastic manner at lower strain amplitudes with a transition point where the elastic and plastic curves cross. It was observed that this transition point never occurred in these specimens with microporosity as the elastic strain amplitudes were always larger than the plastic strain amplitudes. At strain amplitudes of 0.004 and below, plastic strains were virtually nonexistent, and the $\Delta\varepsilon_e/2$ data points can be seen to fall directly on top of the $\Delta\varepsilon/2$ data points.

The cyclic stress-strain curve in Figure 5 for the specimens with microporosity was created using the approximate half-life stable hysteresis loops from various strain amplitudes via the companion method. The curve was formed by connecting the tensile points (loop tips) of the stabilized hysteresis loops obtained at about half life for the strain levels tested as shown in Figure 7. This cyclic stress-strain curve is used to determine material properties which relate the nominal true stress and true strain ranges as given by equation (2).

$$\Delta e = \frac{\Delta S}{E} + 2\left(\frac{\Delta S}{2K'}\right)^{\frac{1}{n'}} \tag{2}$$

The symbols ΔS and Δe are the nominal true axial stress and true axial strain respectively, E is Young's modulus, K' is the cyclic strength coefficient, and n' is the cyclic strain hardening exponent. The value of S_y' was found to be 894 MPa, which is less than S_y, indicating that the material cyclic softened. Cyclic softening commonly occurs with high strength materials and results in softening of the material as the cyclic loading progresses. The majority of softening occurred within the first ten to twenty percent of specimen life, and then slowed to an approximate constant slope of decreasing maximum stress in tension, and increasing minimum stress in compression.

Macroporosity Specimen Fatigue Testing

The fatigue test conditions and test results for all specimens with macroporosity are given in Table 3. They are grouped by "least", "middle" and "most" porosity specimen geometry types, and then from largest to smallest stress amplitude level within each group. Experimental fatigue results of the "least", "middle", and "most" macroporosity levels are shown in comparison to the microporosity specimens in the stress-life, S-N, curve of Figure 8. Scatter bands are drawn around each of the three porosity groups. The scatter bands for the "least" and "middle" porosity groups show significant overlap, indicating that the groups had similar fatigue lives. The scatter band for the "most" porosity group falls farther to the left of the "least" and "middle" porosity groups and has fewer areas of overlap, demonstrating generally lower experimental fatigue lives at the same stress level. Note that all of the macroporosity specimens had considerably shorter fatigue lives than the lives of the microporosity bearing material, and were tested below the microporosity specimens' fatigue limit for the majority of the fatigue testing.

A modulus of elasticity, E_{meas}, of each macroporosity specimen was measured during testing to determine if the porosity level and measured modulus could be correlated. It was also believed that this might serve as an indicator of porosity volume. This "apparent" specimen modulus is reduced from the modulus of sound specimens by the lost section thickness associated with porosity. The modulus of the microporosity test specimens was only 5% lower than the sound data[15] as seen in Table 1, and could be attributable to normal variability and/or the greater microporosity. As can be seen from data in Table 3, the macroporosity specimen modulus values were 20% to 63% lower than the sound material modulus, and 16% to 61% less than the microporosity specimen measured modulus. Measured modulus ranges of 137-153 GPa, 111-166 GPa, and 77-136 GPa were found in the "least", "middle", and "most" specimen groups, respectively. Note that the "least" and "middle" specimen groupings had mean E_{meas} of approximately 144 GPa and produced similar experimental fatigue results, and the mean measured modulus of the "most" specimens was 113 GPa. Both the "least" and "middle" materials had a mean measured modulus significantly higher than the "most" porous material and outperformed the "most" porous specimens in fatigue testing.

Based on the relationship between the measured specimen modulus and fatigue life, a more appropriate grouping of specimens would be on the basis of measured modulus rather than specimen casting geometry. Therefore, new macroporosity groupings based on measured moduli of 140 GPa and greater, 110-139 GPa, and moduli less than 110 GPa were made, approximately splitting the total range of moduli data into thirds. These new groups are plotted in the S-N_f graph of Figure 9 which has scatter bands drawn around the measured modulus groupings. Generally, the data when plotted in these three new groupings show that the higher modulus specimens outperformed the lower modulus specimens, and that categorizing the data based on measured modulus provides a better grouping, with less overlap, than the as-cast geometry did in Figure 8.

All macroporosity tests were conducted using load control. This meant that the amplitude of the axial force on the specimen was determined based on the nominal specimen cross-sectional area and the desired stress amplitude levels prior to testing. The nominal specimen area was determined from diameter measurements made using an optical microscope without consideration of porosity. This test amplitude stress is lower than the true stresses experienced by the specimen material since the specimen area is reduced by the macroporosity. Assuming that the decrease in measured modulus is due to the reduced volume caused by porosity, there is a reduction in then effective cross-sectional area of the specimen test section. Considering this, a better representative value of the "effective" stress amplitude applied to the macroporosity test specimens is calculated by equation (3)

$$S_{calc} = \frac{S_a \cdot E_{micro}}{E_{meas}} \tag{3}$$

where E_{micro} and E_{meas} represent the modulus of the microporosity specimens and macroporosity test specimens respectively, and S_{calc} and S_a represent the newly calculated "nominal" applied stress amplitude, and the original stress amplitude based on a sound test specimen, respectively. Using this equation, the calculated test stress amplitudes ranged from approximately 70-250 MPa

instead of the four stress amplitude groups of 53, 66, 96, and 126 MPa. The calculated stress is given in Table 3 for each specimen test. New data points using the calculated stresses, shown as open shapes, are shown in the S-N_f plot in Figure 10. From Figure 10, the test specimen falls into a power function pattern with the higher stresses generally seeing shorter lives than the lower stresses, as is normally expected with fatigue data. Even with the calculated nominal stress, the specimens with macroporosity still had significantly shorter lives then the microporosity specimens with similar stress amplitudes. It is apparent that using this representative stress amplitude alone does not entirely explain the fatigue behavior of the specimens with macroporosity. The actual stresses responsible for failure are even higher than these calculated stresses. The calculated stresses in Figure 10 are based on a measured modulus arising from the entire specimen test section and are not determined at the failure initiation sites.

Results of the fatigue testing of the micro- and macro- porosity specimens are compared with sound material test curve[15] in Figure 11. Note that the microporosity data (dashed curve) depart more from the sound (solid curve) at decreasing levels of stress, and at lower levels of stress (300 MPa) the fatigue life is reduced by a factor of about 100. Since this microporosity is difficult to detect, it may point to a cause of the overly large safety factor applied to by designers to cast material throughout an entire cast part in lieu of the ability to predict the presence of microporosity in parts and design for its localized effects. The ratio of the stress amplitudes of the microporosity specimens to macroporosity specimens range from 5 at 10^2 cycles to failure to 3 at 10^5 cycles, which emphasizes the dramatically reduced fatigue resistance associated with macroporosity. Runout tests ($N_f > 5x10^6$ cycles) occurred at the 126 MPa stress level in the microporosity test specimens.

The results of the fatigue testing point to the importance of integrating the prediction of porosity in the casting process with the casting design. In the case of microporosity, since it is difficult to detect using NDE, predicting microporosity in the casting process and considering its effect on fatigue life of the part will be useful in designing and producing parts with greater durability and reducing overly large factors of safety applied to design calculations. The results for the macroporosity specimens provide a lower bound or worst case boundary for property. Certainly more research into the effects of macroporosity and an explanation for the significant data scatter observed here is warranted. Unless an engineering approach can be developed to conservatively consider the effects of macroporosity on the casting performance, good casting practices and NDE must be relied upon to prevent it from occurring.

Fractography and Microscopy

Specimens with Microporosity

Following the axial testing, the specimen fracture surfaces were examined with the use of a scanning electron microscope (SEM). The examination revealed two types of cyclic failures for the microporosity specimens. Specimens tested at strain amplitudes greater than or equal to $\varepsilon_a = .003$ showed essentially no fatigue regions and had very rough and jagged fracture surfaces. These are similar to the monotonic fracture surfaces, which despite the low values of percent elongation and percent reduction in area, were widely covered with ductile dimples as shown in Figure 12. Ductile dimples are formed at discontinuities such as second-phase particles,

inclusions, or grain boundaries within the steel and begin to grow and coalesce into cracks that eventually lead to fracture of the component.[19] This microvoid coalescence is typically associated with ductile fracture.

Specimens tested at strain amplitudes below $\varepsilon_a = .003$ had flat regions indicating areas of fatigue crack growth (FCG). Clear regions of crack nucleation and final fracture were also observed in these specimens. The final fracture region was composed primarily of ductile dimples, Figure 12, and the FCG region was composed of fatigue facets. Typical fatigue facets found in the FCG region are shown in Figure 13. Three low strain amplitude specimens were evaluated under the SEM, and all were found to have cracks that nucleated from surface or near-surface porosity approximately 200 μm in diameter such as shown in Figure 14.

Indications of microporosity were not evident in the fracture surfaces at 20 to 3000X magnification nor in the radiographs of the specimens. Therefore the microporosity specimens were sectioned approximately 5 mm behind the fracture surface and ground to mirror surface to reveal widespread presence of micropores. The ground surfaces revealed micropores that were nearly spherical in shape ranging in size from approximately 2-20 μm in diameter. Larger pores on the order of 200 μm as viewed on the fracture surfaces were not evident in these ground sections. The micropores were not spread evenly across the surface; therefore, a conservative estimate of total local micropore volume gathered by measuring the total micropore surface area from a high micropore concentration region is approximately 0.65%. An image of typical micropores found on the ground surface is shown in Figure 15.

Specimens with Macroporosity

Eight specimens with macroporosity were chosen to have their fracture surfaces examined with the SEM. The fracture surfaces fell into two categories: those that showed clear evidence of fatigue fractures such as in Figure 16 (a), and those that did not, Figures 17 (a). Specimens with evidence of fatigue fractures typically had a FCG region as indicated by a large flat region on a macroscopic view, and had the appearance of fatigue facets on a microscopic view. In several specimens, a final fracture region was found on the macroscopic level as a shiny region containing a small but identifiable shear lip. Upon evaluation of the final fracture region on a microscopic level, ductile dimpling was observed as was the case with the microporosity specimens. Unfortunately, none of the specimens showed a clearly identifiable region of crack nucleation at a specific pore. This introduces uncertainty to the application of predictive fatigue models.

Fracture surfaces of the eight specimens selected for study were ground back to more clearly show the porosity present within the specimen. The polished surfaces of the specimens are shown aligned in the same orientation as the fracture surfaces in Figures 16 (b) and 17 (b). The total macropore surface areas of the polished surfaces were then measured revealing levels of porosity ranging from approximately 2.2-30.9%. A calculated porosity percentage was determined from the measured elastic modulus, E_{meas}, of each specimen according to equation (4)

$$\%Porosity = 100\left(1 - \frac{E_{meas}}{E_{micro}}\right) \tag{4}$$

where the constant E_{micro} is the modulus of the specimens with microporosity. The measured pore area percentages are compared to calculated porosity percentages in the third and fourth columns of Table 4. It should be noted that the macroporosity was not uniformly spread throughout the gage section of the specimens. Therefore the measured pore area percentages are not entirely representative of the pore volume of these specimens and are merely a snapshot of a section near the region of fracture. Though their magnitudes are different, the calculated and measured porosities appear to be in relative agreement between specimens.

Modeling Microporosity in Fatigue Life Calculations

Fatigue Life Calculations for Microporosity by Strain-Life Approach

Examination of the fracture and ground surfaces from the specimens with microporosity verified the presence of micropores. The pores responsible for the crack nucleation in the three specimens evaluated were on the order of 200 μm in diameter and were approximately spherical in shape. Due to the round shape of the micropores found within the specimens, the micropore was modeled as a spherical notch with a diameter of 200 μm within the specimen. This notch size is very small compared to the 5 mm diameter of the specimen gage length. Therefore, all of the spherical notches were modeled as being a single notch contained within an infinite body, giving a stress concentration factor, K_t, equivalent to the constant 2.05.[20] This K_t value was then increased by 7%, according to Eubanks,[21] to account for the location of the pore near the surface of the specimen. The final value of K_t was taken to be 2.19.

The stress concentration factor was modified to create a fatigue notch factor, K_f. Fatigue strength depends not only on the stress concentration factor, but also on the notch radius, material strength, and mean and alternating stresses.[22] K_f was determined from K_t using the following equations:

$$K_f = 1 + \frac{K_t - 1}{1 + a/r} \tag{5}$$

$$a = 0.0254 \cdot \left(\frac{2070}{S_u} \right)^{1.8} \tag{6}$$

where, r, is the notch root radius in millimeters, and S_u is the ultimate strength of the material in MPa. It should be noted that equation (6) is applicable to wrought steels. Extending equation (6) to cast steels was the best approximation available for the constant, a.

Fatigue lives of the specimens with microporosity were calculated assuming a micropore notch in sound material. Using the cyclic and fatigue material properties of sound "keel block" specimens,[15] shown in Table 2, a single spheroid notch of 200 μm diameter was chosen to represent the pores which were responsible for failure. Again, this size of pore was found to cause failure in one identifiable case. It is therefore used as a representative pore in these

preliminary calculations to demonstrate how information about the micropore size might be used in determining the effect of microporosity on the steel fatigue resistance. Nominal stresses were calculated at each strain amplitude tested, assuming perfectly sound specimens. This was accomplished using the relationship of equation (2), which relates the nominal true stress and true strain ranges, ΔS and Δe respectively.

The local notch root stress and strain ranges were then calculated from the nominal stress and strain ranges by solving equations (7) and (8) simultaneously, using Neuber's rule and the equation for the stable cycle hysteresis loop, respectively.

$$\Delta\varepsilon \cdot \Delta\sigma = K_f^2 \Delta e \cdot \Delta S \tag{7}$$

$$\Delta\varepsilon = \frac{\Delta\sigma}{E} + 2\left(\frac{\Delta\sigma}{2K'}\right)^{\frac{1}{n'}} \tag{8}$$

Δσ and Δε are the local axial stress and strain at the notch root, respectively. The material properties E, K′, and n′ are those of the sound specimens. The local notch strain range calculated using equations (7) and (8) was then input into equation (1) to determine the approximate life of the specimen. The resulting life calculations are shown in Table 5 and in graphical form in Figure 18, which plots the strain amplitude, ε_a, versus reversals, $2N_f$, to failure. Any notched fatigue life values that were determined to be greater than $5x10^6$ cycles were labeled as run-outs. Specific run-out points were not shown on the graphs, but instead, the life calculation modeling line was extended out to $1x10^7$ reversals.

The results shown in Figure 18 are very encouraging, since micropores responsible for the failure of the specimens with microporosity were determined to be nearly spherical in shape with a diameter of approximately 200 μm and were located at, or near, the surface. Calculations using micropores of this size resulted in reasonably accurate life calculations using the strain-life approach. Examination of the micropore specimen fracture surfaces with a SEM showed that the specimens tested at high strain amplitudes, $\Delta\varepsilon/2 \geq .003$, showed no clear indication of crack nucleation, FCG, or final fracture regions while the specimens tested at low strain amplitudes, $\Delta\varepsilon/2 < .003$, clearly demonstrated all of these features. This may explain the disagreement with the two points at the far left in Figure 18. Since the most useful region of this figure is the high cycle range, these high strain levels would not be desirable in a design or application.

Modeling Micropores by Linear Elastic Fracture Mechanics (LEFM)

Assuming that the fatigue crack growth rate of cracks, da/dN, within the specimens with microporosity follow the relationship modeled by the Paris equation:

$$\frac{da}{dN} = A(\Delta K)^n \tag{9}$$

where A is the intercept of the da/dN axis, ΔK is the mode I stress intensity factor range and n is the slope of the linear region plotted on a log-log scale, linear elastic fracture mechanics was

used to analyze the fatigue test results. Unfortunately, it was not feasible to measure fatigue crack growth properties in the current series of material testing for these microporosity specimens. Therefore, LEFM calculations presented here use properties from the sound specimens, which are given in Table 6. [15]

For fully reversed testing, the value of ΔK was calculated using equation (10):

$$\Delta K = S_{\max}\sqrt{\pi a}F \tag{10}$$

where S_{max} is the maximum stress, a is the crack depth, and F represents a shape factor that relates the geometry of the crack front to the crack depth. Equation (10) only takes into account S_{max} because the minimum stress intensity factor is undefined in compression and will have a value of zero. Additional crack closure was not incorporated. Inputting equation (10) into equation (9) and integrating from the initial crack depth, a_i, to the final crack depth, a_f, produces equation (11), giving the total cycles to failure.

$$N_f = \int_0^{N_f} dN = \int_{a_i}^{a_f} \frac{da}{A\left(S_{\max}\sqrt{\pi a}F\right)^n} \tag{11}$$

Cracks responsible for the failure of the specimens were formed from 200 μm diameter pores located near or at the surface of the round specimens. Therefore, the cracks were modeled as semi-circular surface cracks. Forman created a model for semi-circular cracks growing in round bars, much like the cracks growing in the these specimens.[23] Using this model, where D is the diameter of the round specimen, the shape factor F(a/D) becomes:

$$F\left(\frac{a}{D}\right) = g\left(\frac{a}{D}\right)\left[0.725 + 2.02\frac{a}{D} + 0.37\left(1-\sin\left(\frac{\pi}{2}\frac{a}{D}\right)\right)^3\right] \tag{12}$$

$$g\left(\frac{a}{D}\right) = 0.92\left(\frac{2}{\pi}\right)\left[\tan\left(\frac{\pi}{2}\frac{a}{D}\right)/\left(\frac{\pi}{2}\frac{a}{D}\right)\right]^{\frac{1}{2}}/\cos\left(\frac{\pi}{2}\frac{a}{D}\right) \tag{13}$$

The method used to determine the initial crack length was to take the square root of the projected area of the pore that nucleated the crack.[10,12] Therefore, an initial crack length of 177 μm was used for the micropore specimens, since the micropores that nucleated the cracks leading to fracture had a diameter of 200 μm. This assumed initial crack length is termed "physically small" by ASTM Standard E647, since it is less than 1 mm.[24] Five of the eight stress levels resulted in ΔK below the long crack threshold stress intensity factor, ΔK_{th}, so small crack growth behavior was assumed to exist. Since small crack growth behavior was not evaluated for the sound specimens, this growth was calculated by extrapolating equations (9 and 11) into the small crack growth region from the sound data.[15] The specimens tested at strain amplitudes greater than $\varepsilon_a = .0015$ were run in strain control, so the stable cycle stress taken from mid-life of the specimen was used as an approximation of S_{max}. The maximum stress used during testing

must be less than or equal to eight-tenths the yield strength for LEFM to be applicable. Therefore, two of the testing levels, ε_a = .01 and ε_a = .008, could not be evaluated with this procedure since the stable cycle tensile peaks were too large and violated LEFM restrictions.

The final crack length of each specimen was determined from the point where net section yielding would occur, or the critical stress intensity factor, K_c, was reached. However the Forman crack front model is only capable of reaching crack sizes equivalent to the radius of the specimen, as is demonstrated by the following equation for determining the crack length:

$$r = \frac{a(2R-a)}{2(R-a)} \tag{14}$$

where r the radius of the circle describing the crack front and the specimen radius is R. As the crack length, a, approaches R, the equation becomes undefined. If net section yielding could only be reached when a crack length larger than R was reached, the crack shape was assumed to become a straight front, so net section yielding, and consequently, a_f, was calculated. However, equations (12) and (13) were still used to calculate the stress intensity factor. It was found that all failures occurred by net section yielding.

Table 7 gives specimen test information, and the experimental and calculated fatigue lives using the Forman crack front model. These results are compared in Figure 19. Note that the calculations modeling the micropores as a crack overestimate of the experimental life, and five of the eight strain amplitudes were not capable of producing a stress intensity factor that was above the long crack threshold intensity factor of ΔK_{th} = 9.4 MPa$\sqrt{m}$ for the given crack size. However, small crack growth can occur below this ΔK_{th}. Though the model indicates that the initial discontinuities would not have led to specimen failure if they were treated as long cracks, evaluation of the fracture surface indicated that the near surface porosity did indeed contribute to the failure.

Small crack growth is greatly influenced by the microstructure of the component and is often very unpredictable. It can be approximated by the extrapolation of the Paris equation into small crack growth region behavior. This extrapolation of the Paris equation may have contributed to the inaccuracies produced when calculating small crack growth behavior. Other sources of error include the use of material properties that were not directly gathered from the specimens with microporosity. Compared to sound material, specimens with microporosity likely have a lower threshold value and a faster crack growth rate at a given ΔK due to stress concentrations created around microvoids within the material. Shorter calculated specimen life is caused by either shifting the Paris equation up, increasing the constant A, or increasing the slope of the equation, raising the value of the constant n, which would lead to shorter calculated specimen life.

Fatigue Life Calculations for Macroporosity

Macroporosity Fatigue Life Calculations by Strain-Life Approach

To calculate the fatigue life of the macroporosity specimens using the strain-life approach, the appropriate notch model must be selected, in addition to size and shape data for the notch responsible for the failure. Since it was not possible in this study to identify the particular notches responsible for the failures of the macroporosity specimens, the course of action taken was to perform preliminary test calculations using the notch models available with notch (pore) size and shape data determined from microscopy. In the preliminary test calculations that follow, the best representative notch model results determined in this study are presented.

Spherical, hemispherical or 3-D ellipsoidal notches, the Sadowsky/Sternberg or the Neuber notch models could be used to model the stress concentration factors. In the current work, these stress concentration factors were determined from best fit lines to the curves found in the handbook of stress concentration factors by Peterson.[20] These assume the notch to be internal in an infinite body and so the surface stress concentration factor, K_t, was increased by 7% as mentioned earlier. Notch size and shape data are required to develop a "model" notch within the material, and this was determined from microscopy. All notch models in Peterson's handbook were explored.[20] Based on the microscopy work, specimen C4 was determined to be a good representative specimen for the purpose of applying strain-life calculations. In specimen C4, the macroporosity was encapsulated at the specimen center and did not extend as near the surface as it did in some specimens. Specimen C4 had three large macropores on the ground-back fracture surface. Based on the average dimension of the pores in C4, a spherical notch of radius 0.75 mm was selected as the representative notch. The cross sectional area of this notch was close to the average pore area in specimen C4. Lastly, using the spherical notch model[20] fore this size of notch gave agreement between calculated and measured fatigue life.

Results of the life calculations are compared with measured lives in Figure 20 using this "representative" 0.75 mm radius notch in all specimens. Note that the data point for specimen C4 is indicated in the figure. Using this identical notch size in all specimens, the only other variables reflecting the different amounts of porosity in each specimen are E_{meas} and S_{calc}. Macropores cause a substantial loss of cross-sectional area within the specimen, and hence a large increase in the applied stress. Considering this, the calculated stress from equation (3) was used as the stress amplitude in the strain-life modeling. Agreement between measurement and calculation is good for about two-thirds of the specimens in Figure 20, and poor for the other third. Also, where there is disagreement, it is unfortunately non-conservative. Eight specimens (circled in Figure 20), four of which are above the upper 10X life interval line, were selected for detailed analysis to see if using more scrutiny in the selection of the notch model, and the notch dimensions, would produce better agreement. These eight specimens are listed in Table 4. Note that these eight specimens were tested over a range of stress amplitude levels. Specimens C10 and E6 were chosen for detailed analysis specifically for their unusually long and short lives, respectively. Each macroporosity casting group was represented in the eight selected specimens.

The Sadowsky/Sternberg type notch was used for pores that loosely resembled the shape of a cigar or American football. Pores of this type required measurements of the major and

minor axis, which were determined by microscopy of the 2-D polished surface images. The Neuber notch more effectively modeled pores that were disk shaped. The plane of the ellipse is parallel to the loading direction for the Neuber notch with the axis of revolution about the minor axis. Also, depth of the pore is needed to obtain the length of the minor axis, and hence the dimension could not be gathered from the 2-D images of the polished specimen surface. Using these notch models the stress concentration factors, K_t, ranged from 2.27-2.97. From K_t, a fatigue notch factor was calculated using equations (5) and (6). Table 4 contains the ellipsoidal notch information used in the specimens selected for analysis: notch type, major and minor ellipse axis length, K_t and K_f. In cases where a specimen contained multiple pores, the notch was created to fit the dimensions of the largest pore on the ground surface of the specimen.

Using S_{calc} from equation (3), the nominal strain ranges were determined through the relationship of equation (2)**,** and the notch root strain was determined from equations (7) and (8). The specimen life was calculated using equation (1), with the results shown in Table 8. Calculated versus experimental fatigue lives are shown in Figure 21 using solid data points for strain-life modeling. Generally, the calculations are still seen again to be non-conservative. The effectiveness of the local strain-life model with ellipsoidal notches in calculation of the fatigue life of specimens with macroporosity varied significantly. For specimens where there was agreement with measurements, no remarkable differences were observed during microscopy between those specimens and the specimens that were in poor agreement. Unfortunately, the agreement was achieved only by coincidence.

Several assumptions were made in the model calculations, and there were difficulties that should be noted. Though many macropores were evident throughout the ground surfaces of some of the specimens, the fatigue life calculation only takes into account the influence of a single pore, or tightly spaced group of pores modeled as a single ellipsoidal notch. Strain-life material properties from the specimens with microporosity were used in the fatigue life calculations for the specimens with macroporosity. These material properties used are given in Table 2. This is believed to be an accurate representation of the specimens with macroporosity because the "sound" portions of the specimens were observed to contain micropores ranging from approximately 10-300 μm in diameter. Essentially, the macropore notches reside within material having properties of the specimens with microporosity. Recall that the notch models assume an infinite body. However, as is evident in Figures 16 and 17, the macropores are of a size comparable to the nominal area of the specimen. Therefore another shortcoming of the calculations is that the "corrected" infinite body solution does not accurately reflect the true K_t of these specimens.

Fundamental factors that may explain the disagreement between the calculations and measurements of the macroporosity specimens are: complex pore shape, an inability to determine a specific pore responsible for failure, the use of infinite body notch models, the use of specimens with microporosity to provide material properties, and the use of a calculated stress based on the modulus, E_{meas}. The shape of the porosity was very torturous and made the process of fitting a notch to the pore geometry difficult and not entirely quantitative. This led to uncertainty in the notch dimensions which resulted in the poor agreement of the life calculations. The pores were also very large in relation to the overall dimension of the specimens. It may have been beneficial to use larger specimens or create specimens with smaller amounts porosity

present. Either case would eliminate the doubt of using the infinite body model, as well as reduce the necessity of using a value such as S_{calc} for a stress input into the life calculation equations.

Modeling Macropores by LEFM Approach

Modeling the fatigue lives of the eight selected specimens listed in Table 4 by LEFM was also performed. It could not be determined which pores were responsible for the failure of a particular specimen through fractographic analysis. Therefore, the square root of the total surface area of the porosity was used to determine the initial crack length for each specimen as measured. It was anticipated that this approach would give a conservative estimate and would be valid for the life calculation modeling. The crack length at fracture was determined to be the point of net section yielding and was determined in the same manner through which a_f for the micropore modeling was found. The value of ΔK was determined using equations (10), (12), and (13) and the maximum nominal stresses encountered during testing. The Forman crack front model, equations (12) and (13), was again used due to the presence of surface porosity on all of the evaluated specimens, though actual crack nucleation regions could not be determined. The life calculation was made by numerically integrating equation (11), with the results shown in Table 9.

The calculated LEFM fatigue lives versus the experimental fatigue lives are shown in Figure 21 as open data points. The LEFM life calculations produced results that were generally in less agreement than the notched strain-life calculations. Only one of the LEFM life calculations was conservative, with four specimens having calculated lives more than ten times longer than what was observed experimentally. The initial crack length was taken as the square root of the total pore surface area found on the ground surface instead of just a single pore or group of pores that were thought to be responsible for the failure of the specimen, which should have led to conservative results. As with modeling the micropores, the use of crack growth properties taken from sound (keel block) material may have affected the life calculations of the specimens with macroporosity. Assumptions that may have adversely affected the model calculations are: modeling macropores as the square root of the total pore area, uncertainty in the actual macropore sizes responsible for failure, and the lack of good crack front propagation models for material surrounding the macroscopic pore.

Discussion

Cyclic and fatigue material properties were measured through strain and load controlled R = -1 testing of the microporosity specimens. Microporosity specimens had low $\Delta\varepsilon_p/2$ at high strain amplitudes and virtually no $\Delta\varepsilon_p/2$ at strain amplitudes lower than $\Delta\varepsilon/2 = .006$. The fatigue limit, S_f, was also much lower than sound cast material. The difference in material properties was due to the occurrence of microporosity. Comparison of the micropore cast steel material with sound specimen properties revealed similar monotonic strengths, but reduced ductility. Percent reduction in area was significantly reduced by approximately a factor of four, and though a direct comparison between percent elongation was not possible, a value of 2.5% would be considered very low for cast steels of similar strength which normally have a percent elongation

near 20%. Microporosity had a significant influence on the cyclic and fatigue properties of the specimens with microporosity. The reduced ductility of the steel led to a lack of plastic strain observed during cycling, causing the elastic strain amplitudes to remain larger than the plastic strain amplitudes at all strain levels tested. This would cause the material to behave in a more brittle manner with increased crack growth rates and consequently reduced fatigue strengths at all strain amplitudes. Evidence of this is shown in the reduced fatigue limit at $5x10^6$ cycles which is less than half of the S_f observed in the sound specimens. Further, the micropores themselves would act as stress risers within the specimen, further decreasing the crack nucleation times.

Specimens containing macroporosity performed significantly poorer than specimens that contained microporosity in fatigue testing. For a stress amplitude of 126 MPa, the two specimens with microporosity resulted in runout tests; their fatigue were lives greater than 5 x 10^6 cycles. At the same stress level eight macroporosity specimens in all three groups were tested, and the lives of these specimens ranged from 160 to 41,000 cycles. Within the three macroporosity specimen groups, the "least" and "middle" porosity groups were found to have similar fatigue lives and both outperformed the "most" porosity group. A correlation between the measured specimen modulus, E_{meas}, the porosity level (represented by specimen group), and the specimen fatigue life was observed. The specimen modulus, E_{meas}, was shown to have a strong correlation with the fatigue life of the specimens and was subsequently used as a new way of grouping the specimens. Generally, specimens with higher E_{meas} outperformed the lower modulus specimens, but significant scatter could still be observed within the modulus groups, particularly noticeable in the modulus 110-139 GPa grouping, as well as in the calculated stress grouping. E_{meas} appears to be a better indicator of fatigue performance than specimen grouping, but this information alone can not be accurately correlated to the life of a specimen.

The most common size of pore found on ground surfaces within of specimens with microporosity was approximately 8 μm in diameter. However, sizes up to 20 μm in diameter were also observed. Larger pores, on the order of 200 μm in diameter, were observed on several of the specimen fracture surfaces. Though these larger pores may not be numerous within the current material, they have a significant influence on the fatigue life. From local strain-life modeling, a notch diameter of 200 μm gave good agreement with fatigue testing. LEFM modeling of micropores did not produce accurate life calculations due to the small crack growth behavior of the micropores and lack of crack growth property data.

Due to the small size of the micropores, the extent of microporosity could not be determined conclusively, neither by examination of the radiographs nor through the examination of the fractures surfaces. Information on the size and distribution of microporosity was gathered through microscopy conducted on ground surfaces of the microporosity specimens. The total microporosity area was determined to be 0.65% or less within the microporosity specimens. This relatively small percentage of microporosity caused significant reduction in ductility performance, which concurs with a study by others who found that microporosity values greater than 0.5% significantly reduced percent elongation and percent reduction in area while having little effect on strength properties.[25]

Life calculations for the specimens with macroporosity provided primarily non-conservative results and differed from the experimental life by nearly two orders of magnitude for both the strain-life and LEFM approaches. Modeling the effect of macroporosity using the strain-life approach is hampered by the torturous shape of the shrinkage porosity and the large size of the macropores relative to the specimen diameter. Determining a proper value for Kt is difficult. Also, modeling the effect of macroporosity using LEFM produced inaccurate results possibly from using crack growth properties taken from different material testing, as well as the large size of macroporosity located within the specimens. Examination of the porous material fracture surfaces with the SEM showed that many specimens had no clear indication of crack nucleation, FCG, or final fracture regions on either the micro or macroscopic levels. Several specimens tested did have FCG and final fracture regions similar to the micropore material low strain amplitude specimens on both the micro and macroscopic levels, no clear indication of crack nucleation could be determined.

Summary and Conclusions

Cast steel containing a variation in porosity from micro- to macro- levels were tested for strength and fatigue and the results were then compared with fatigue calculation models. Radiographic analysis of the specimens of the specimens with microporosity gave no indications of porosity within the specimens, while the “least” and “middle” porosity groups appeared to contain similar amounts of porosity, and the “most” porosity group contained the highest porosity.

Based on the preliminary calculations performed here, there is evidence that using strain-life models for cast steel with microporosity can provide the engineering approach sought to couple casting simulation prediction of porosity with the prediction of part fatigue performance. Since microporosity is not usually detected by radiography (or other NDE), the possibility of its presence in parts can be considered in the design process either by “what-if” analysis, or by integrating casting process simulations with the design analyses. When the fatigue test results for both the micro- and macro-porosity specimens are compared with sound keel block data, the full range of mechanical property degradation caused by porosity is seen. The issues which are believed to prevent good calculation for the macroscopic specimen continue to be investigated, and quantitative analysis of radiographs of the specimens made prior to testing are being analyzed and compared with the test results to assist in these investigations. This will be the subject of a future report since it is beyond the scope of the present work.

Acknowledgments

This research was undertaken as part of the Integrated Design of Steel Castings for Service Performance project which is funded by the United States Department of Defense through the American Metalcasting Consortium (AMC) PRO-ACT program. AMC’s PRO-ACT program is sponsored by Defense Supply Center Philadelphia (DSC, Philadelphia, PA) and the Defense Logistics Agency (DLA, Ft. Belvoir, VA). This research is also conducted under the auspices of the Steel Founders' Society of America, and through substantial in-kind support, guidance and interest from SFSA member foundries. In particular, we would like to thank Harrison Steel for several trial iterations of test specimens and the final test specimen castings,

Alloy Weld Inspection Co. for their digital and film radiography of the fatigue test specimens, and MAGMA GmbH for their support of the porosity prediction model used to design the test specimen castings. Any opinions, findings, conclusions, or recommendations expressed herein are those of the authors and do not necessarily reflect the views of DSC, DLA, or the SFSA and any of its member foundries.

References

1. Standard E446, "Reference Radiographs for Steel Castings up to 2 inches (51 mm) in Thickness", *2002 Annual Book of ASTM Standards* (American Society of Testing and Materials, West Conshohocken, PA 2002), **Vol. 03.03**, 189-191.

2. Standard E186, "Standard Reference Radiographs for Heavy-Walled 4 ½ to 12-in. (114 to 305-mm) Steel Castings", *2002 Annual Book of ASTM Standards* (American Society of Testing and Materials, West Conshohocken, PA 2002), **Vol. 03.03**, 81-83.

3. Standard E280, "Standard Reference Radiographs for Heavy-Walled 2 to 4 ½-in. (51 to 114-mm) Steel Castings", *2002 Annual Book of ASTM Standards* (American Society of Testing and Materials, West Conshohocken, PA 2002), **Vol. 03.03**, 125-127.

4. M. Kohno, M. Makioka, "Some Studies on the Manufacture of Cast 13 Chrome Stainless Steel Francis Type Runners for Hydraulic Turbines", *AFS Transactions*, 1970, 9-16.

5. K. Chijiwa, T. Nakayama, M. Imamura, "Effect of Casting Defects upon the Endurance Limit of Large Steel Casting", *35e CIF*, **36**, 1-12.

6. J. G. Conley, B. Moran, J. Gray, "A New Paradigm for the Design of Safety Critical Castings", *Aluminum in Automotive* Applications (SAE Special Publications, 1998), **Vol. 1350**, 25-38.

7. Q. G. Wang, D. Apelian, D. A. Lados, "Fatigue Behavior of A356-T6 Aluminum Cast Alloys. Part I. Effect of Casting Defects", *Journal of Light Metals*, 2001, **1**, 73-84.

8. C. M. Sonsino, J. Ziese, "Fatigue Strength and Applications of Cast Aluminum Alloys with Different Degrees of Porosity", *International Journal of Fatigue*, 1993, **15(2)**, 75-84.

9. P. Heuler, C. Berger, J. Motz, "Fatigue Behaviour of Steel Castings Containing Near-Surface Defects", *Fatigue & Fracture of Engineering Materials & Structures*, 1992, **16(1)**, 115-136.

10. S. Jayet-Gendrot, P. Gilles, C. Migne, "Behavior of Duplex Stainless Steel Casting Defects Under Mechanical Loadings", *Fatigue and Fracture Vol.1* (American Society of Mechanical Engineers, Pressure Vessels and Piping Division, 1997), **Vol. 350**, 107-116.

11. T. Mansson, F. Nilsson, "Fatigue Life Estimation of Cast Components", *International Journal of Cast Metals Research*, 2001, **13(6)**, 373-378.

12. P. Hausild, C. Berdin, P. Bompard, N. Verdiere, "Influence of Shrinkage Cavities on Fracture Behaviour of Duplex Stainless Steel", *Materials Science and Engineering A*, 2002, **335(1-2)**, 164-174.

13. R. Hardin and C. Beckermann, "Effect of Shrinkage on Service Performance of Steel Castings", *2002 SFSA Technical and Operating Conference Proceedings*, 2002.

14. K.D. Carlson, Z. Lin, R.A. Hardin, C. Beckermann, G. Mazurkevich and M.C. Schneider, "Modeling of Porosity Formation and Feeding Flow in Steel Casting", *Proceedings of Modeling of Casting, Welding and Advanced Solidification Processes X*, (May 25-30, Destin, Florida, 2003), 295-302.

15. R. I. Stephens, *Fatigue and Fracture Toughness of Five Carbon or Low Alloy Cast Steels at Room or Low Climatic Temperatures* (Carbon and Low Alloy Technical Research Committee, Steel Founders' Society of America, Des Plaines, IL, 1982).

16. Standard E606, "Standard Practice for Strain-Controlled Fatigue Testing", *2002 Annual Book of ASTM Standards* (American Society of Testing and Materials, West Conshohocken, PA 2002), **Vol. 03.01**, 569-583.

17. Standard E1012, "Standard Practice for Verification of Specimen Alignment under Tensile Loading", *2002 Annual Book of ASTM Standards* (American Society of Testing and Materials, West Conshohocken, PA 2002), **Vol. 03.01**, 738-745.

18. Standard E08, "Standard Test Methods for Tension Testing of Metallic Materials", *2002 Annual Book of ASTM Standards* (American Society of Testing and Materials, West Conshohocken, PA 2002), **Vol. 03.01**, 60-81.

19. C. R. Brooks, A. Choudhury, *Failure Analysis of Engineering Materials* (McGraw-Hill, New York, 2002).

20. R. E. Peterson, *Stress Concentration Factors* (Wiley-Interscience, New York, 1974).

21. R. A. Eubanks, "Stress Concentration Due to a Hemispherical Pit at a Free Surface", Trans. ASME, **76**, Appl. Mech. Section, 57-62.

22. R. I. Stephens, A. Fatemi, R. R. Stephens, H. O. Fuchs, *Metal Fatigue in Engineering* (2nd Edition, Wiley-Interscience, New York, 2000).

23. R. G. Forman, V. Shivakumar, "Growth Behavior of Surface Cracks in the Circumferential Plane of Solid and Hollow Cylinders", *Fracture Mechanics: Seventeenth Volume, ASTM STP 905* (ASTM, Philadelphia, 1986), 59-74.

24. Standard E647, "Standard Test Method for Measurement of Fatigue Crack Growth Rates." *2002 Annual Book of ASTM Standards* (American Society for Testing and Materials, West Conshohocken, PA, 2002), **Vol. 03.01**, 603-644

25. J. A. Griffin, R. D. Griffin, C. D. Pears, "Correlation of Tensile Properties to Niyama and Fracture Surface Anomalies", *2002 SFSA Technical and Operating Conference Proceedings*, 2002.

Table 1 - 8630 Steel Monotonic Properties

Property	Micropore Material Avg.	Sound Material[15]
S_u (MPa)	1 125	1 144
S_y (MPa)	1 088	985
E (GPa)	197	207
%EL	2.5	----
%RA	7.0	29
σ_f (MPa)	1 156	1 268
ε_f	.073	.35
K (MPa)	1 307[#]	----
n	.0279[#]	----

[#] Not the arithmetic mean but the best fit regression to the aggregate data

Table 2 - 8630 Steel Cyclic Properties

Property	Micropore Material	Sound Material[15]
S_f (MPa)	126	293
S_f/S_u	.11	.26
K′ (MPa)	2 550*	1 502 / 2 267[#]
n′	.167*	.122 / .195[#]
S_y' (MPa)	894*	682 / 661[#]
b	-.176	-.121
c	-.908	-.693
σ_f' (MPa)	2 390	1 936
ε_f'	.11	.42

* Data determined from the companion method

[#] Data determined from the companion and incremental step methods respectively

Table 3 – Macroporosity Specimen Load Control Test Data and Results

Specimen ID	Porosity Level	Stress Amp (MPa)	N_f	E (GPa)	Calculated Stress (MPa)
C4	Least	126	24 320	143	174
C8	Least	126	29 023	153	163
C2	Least	96	1 365	137	138
C3	Least	96	79 908	149	127
C9	Least	66	216 516	145	90
C10	Least	66	4 053 800	141	92
C5	Least	53	851 275	138	76
H8	Middle	126	7 456	148	168
G5	Middle	126	13 013	142	175
H3	Middle	126	40 896	155	161
G2	Middle	96	4 392	111	171
G8	Middle	96	41 066	125	152
H7	Middle	96	333 025	142	134
H2	Middle	66	769 074	151	86
G1	Middle	66	1 681 018	166	79
G7	Middle	53	249 752	143	73
G4	Middle	53	1 342 218	145	72
E6	Most	126	160	120	207
E8	Most	126	11 648	136	183
D6	Most	126	37 089	135	184
E1	Most	96	1 935	90	211
E5	Most	96	6 042	77	246
D10	Most	66	15 419	113	115
D4	Most	66	57 566	135	97
D8	Most	66	113 503	136	96
D5	Most	53	10 812	87	120
E10	Most	53	15 868	104	101

Table 4 – Measured Macropore and 3-D Notch Geometries

				Ellipsoidal Notch Information				
Specimen	Young's Modulus, E (GPa)	Calc. Porosity (%)	Meas. Pore Area (%)	3-D Notch Type	Major Axis, 2a (mm)	Minor Axis, 2b (mm)	K_t	K_f
H2	151	23.4	14.9	Neuber	2.25	1.8	2.36	2.23
G7	143	27.4	2.2	SS	2.01	0.43	2.82	1.70
C4	143	27.4	10.5	SS	1.50	0.75	2.47	2.05
C10	141	28.4	13.5	Neuber	1.75	1.00	2.97	2.56
C2	137	30.5	23.2	SS	3.33	1.15	2.66	2.21
E6	120	39.1	27.6	Neuber	2.35	2.00	2.27	2.17
E1	90	54.3	29.7	SS	4.10	1.79	2.54	2.30
D5	87	55.8	30.9	SS	4.00	2.35	2.37	2.24

Table 5 - Calculated Lives for a 200 μm Spheroidal Notch Using The Local Strain-Life Model Compared with Microporosity Material

ε_a	Micropore Material N_f (Cycles)	200 μm Notch N_f (Cycles)
.01	10	27
.008	29	40
.006	153 / 381	70
.004	3 800	170
.003	650 / 3 476	300
.002	19 299	2 100
.0015*	62 112	11 800
.001*	517 015 / 512 858	222 000
.0008*	951 965	1 240 000
.00065*	Run-Out[#] / Run-Out	Run-Out

* Strain amplitude approximated using load control

[#] Run-out was taken as 5 000 000 cycles

Table 6 – Crack Growth Properties

Property	Data Used for Calculations
S_y (MPa)	1088
ΔK_{th} (MPa$\sqrt{m}$)	9.4*
K_c (MPa$\sqrt{m}$)	135*
A (m/cycle)	2.63×10^{-12}*
n	3.03*

* Properties from sound material[15] at R=0

Table 7 – Results of Modeling a Single 200 μm Diameter Pore as a Surface Crack

S_{max} (MPa)	Net Section Yielding (%)	Experimental N_f (cycles)	a_f (mm)	Calculated N_f (Cycles)
862	79.2	153 / 381	1.57	27 400
790	72.6	3 800	1.80	35 700
698	64.2	6 50 / 3 476	2.07	51 900
395	36.3	19 299	3.04	291 000[#]
296	27.2	62 112	3.42	699 000[#]
198	18.2	517 015 / 512 858	3.81	2 360 000[#]
158	14.5	951 965	3.98	4 680 000[#]
126	11.6	Run-Out* / Run-Out	4.15	Run-Out[#]

* Run-Out is 5×10^6 cycles

[#] Small crack growth assumption was needed to make life predictions

Table 8 – Results of Modeling Macropores as Ellipsoidal Notches Using the Local-Strain Model

Specimen	Stress Amplitude, S_a (MPa)	Calculated Stress, S_{calc} (MPa)	Young's Modulus, E (GPa)	Experimental N_f (Cycles)	Calculated N_f (Cycles)
H2	66	86	151	769 074	834 000
G7	53	73	143	249 752	Run-Out*
C4	126	174	143	24 320	24 500
C10	66	92	141	4 053 800	295 000
C2	96	138	137	1 365	60 275
E6	126	207	120	160	6 800
E1	96	211	90	1 935	4 333
D5	53	120	87	10 812	124 000

* Run-Out is 5 x 10^6 cycles or greater

Table 9 – Results of Modeling Macropores as a Crack

Specimen	S_{max} (MPa)	Experimental N_f (cycles)	a_i (mm)	a_f (mm)	Calculated N_f (Cycles)
H2	66	769 074	1.70	4.44	1 080 000[#]
G7	53	249 752	0.66	4.52	Run-Out*[#]
C4	126	24 320	1.44	4.13	294 000
C10	66	4 053 800	1.63	4.44	1 320 000[#]
C2	96	1 365	2.14	4.28	119 000
E6	126	160	2.33	4.13	31 400
E1	96	1 935	2.41	4.28	56 400
D5	53	10 819	2.46	4.52	298 000[#]

* Run-Out is 5 x 10^6 cycles or greater

[#] Stress intensity threshold value was not exceeded

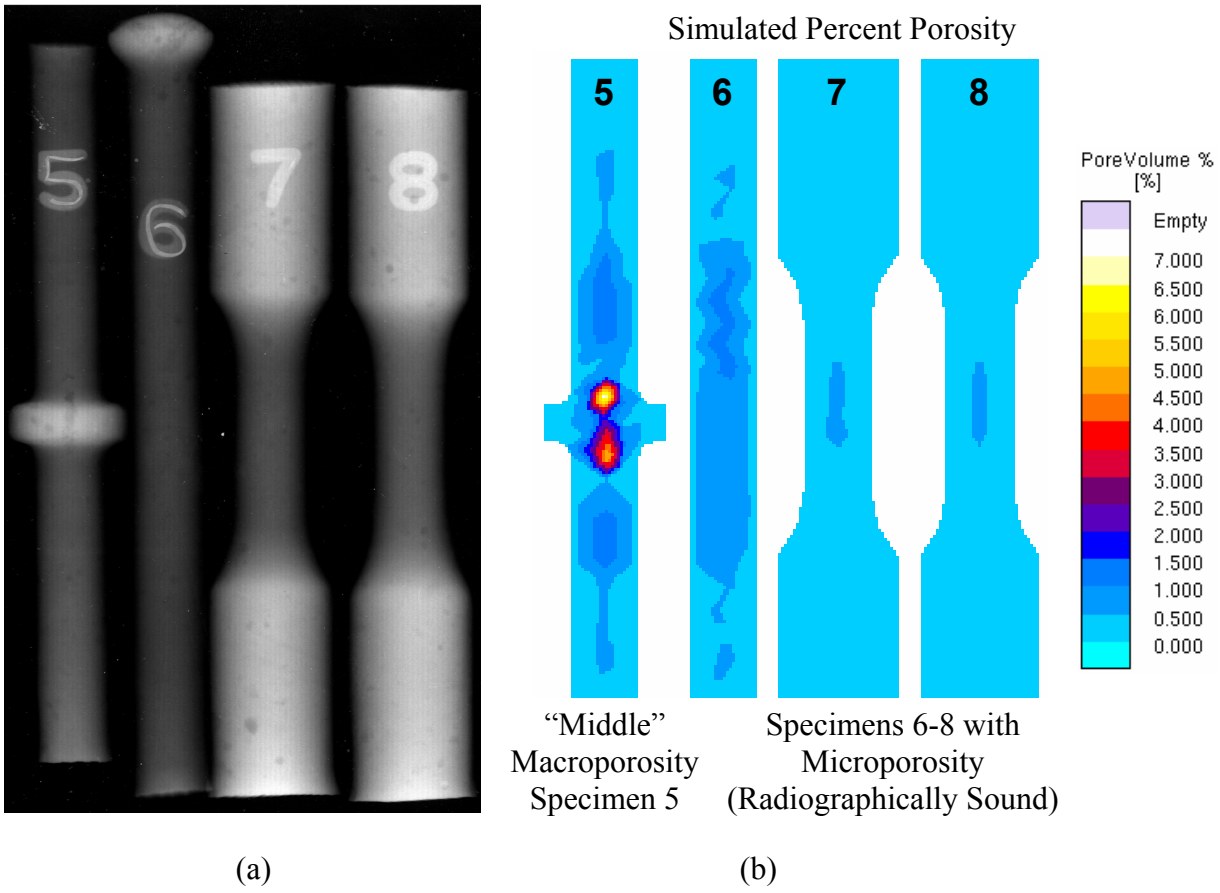

Figure 1 - Typical comparison between (a) radiographs of specimens and (b) computer model predictions of specimen porosity volume percentage

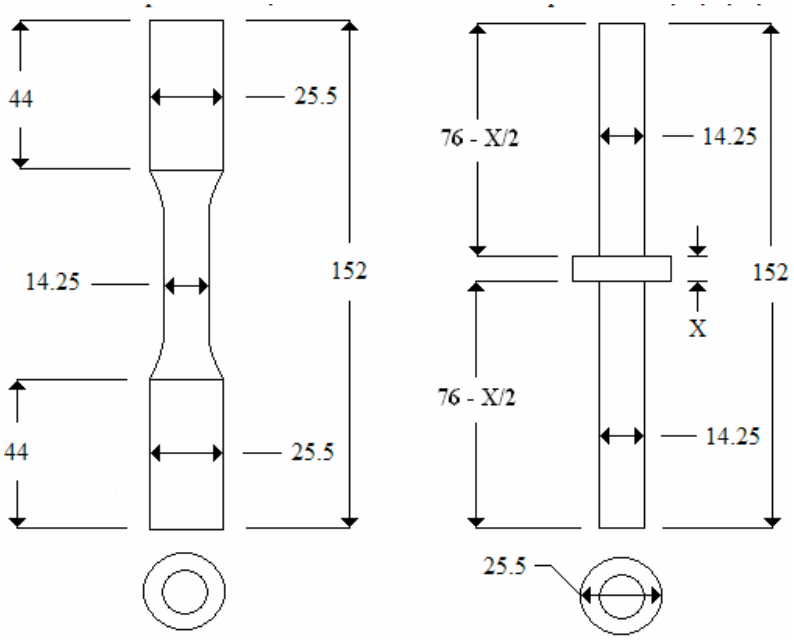

(a) Microporosity Specimen Blanks (b) Macroporosity Specimen Blanks

Figure 2 - Dimensions of cast blanks in millimeters. Dimension "X" = 5, 7.5, and 10 mm for the "least", "middle", and "most" macroporosity specimen groups respectively.

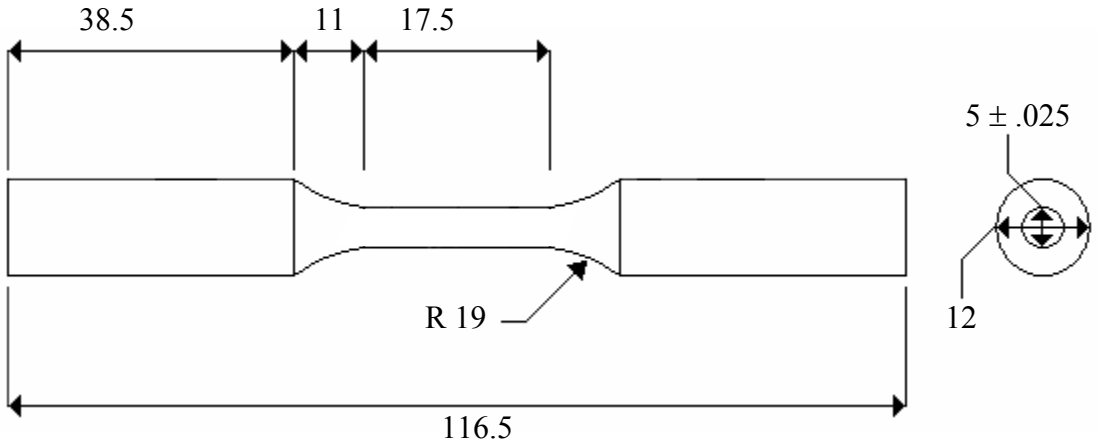

Figure 3 - Final dimensions of fatigue specimens in millimeters

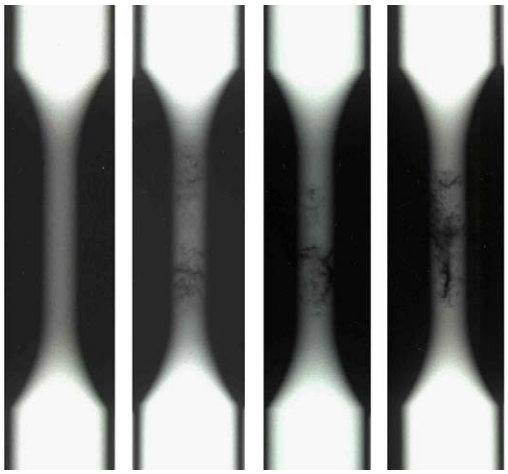

Figure 4 - Radiograph images of the (a) microporosity specimens, (b) “least” macroporosity specimens, (c) “middle” macroporosity specimens, and (d) “most” macroporosity specimens

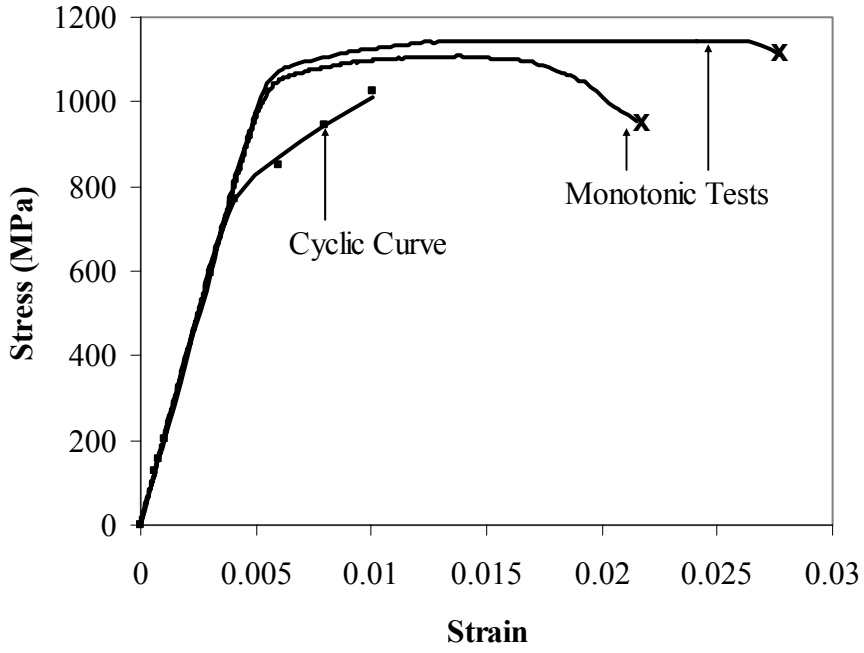

Figure 5 - Monotonic and cyclic stress-strain curves of microporosity specimens

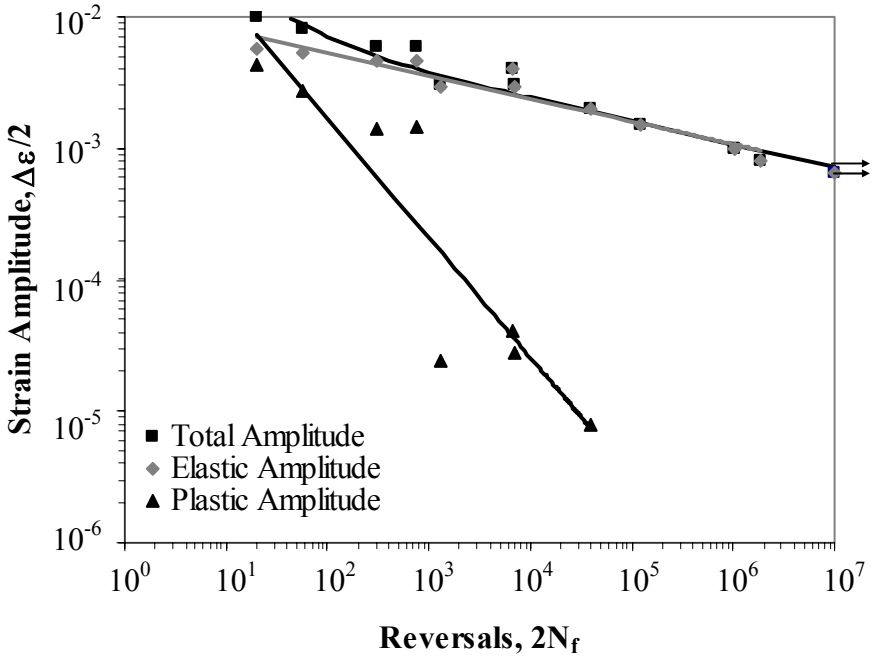

Figure 6 - Total, elastic, and plastic strain-life curves of microporosity specimens

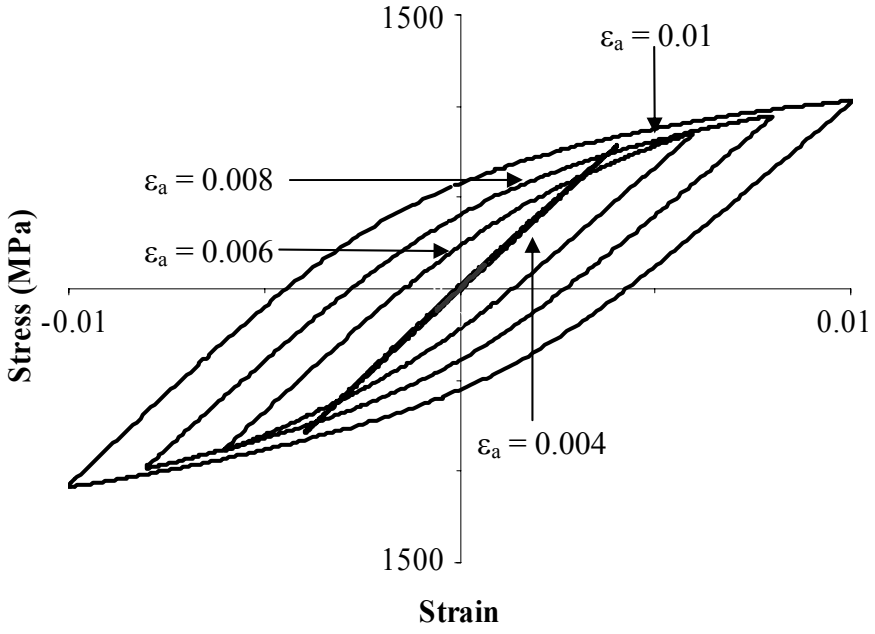

Figure 7 - Half-life hysteresis loops used to create the cyclic stress-strain curve

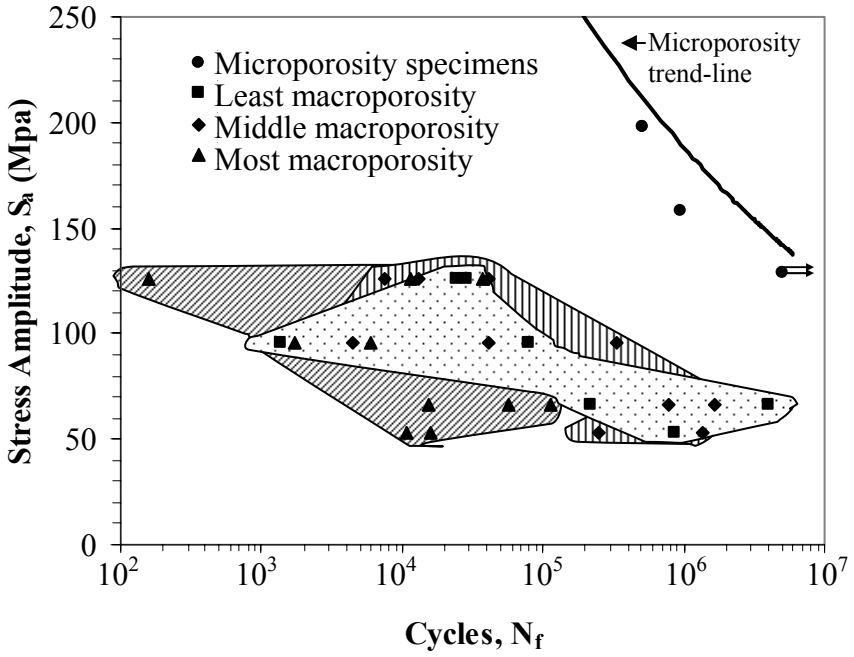

Figure 8 - Porous material fatigue data with scatter bands. ( ) "least" porosity ( ) "middle" porosity, ( ) "most" porosity

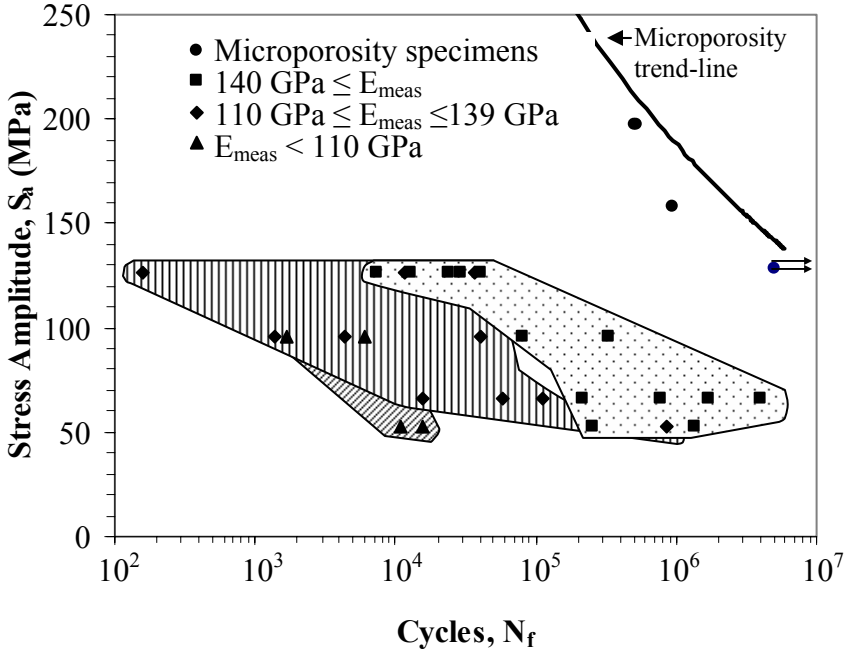

Figure 9 - Porous material fatigue data grouped by modulus, E_{meas}, with scatter bands. ( ) modulus 140 GPa and greater, ( ) modulus 110-139 GPa, ( ) modulus less than 110 GPa

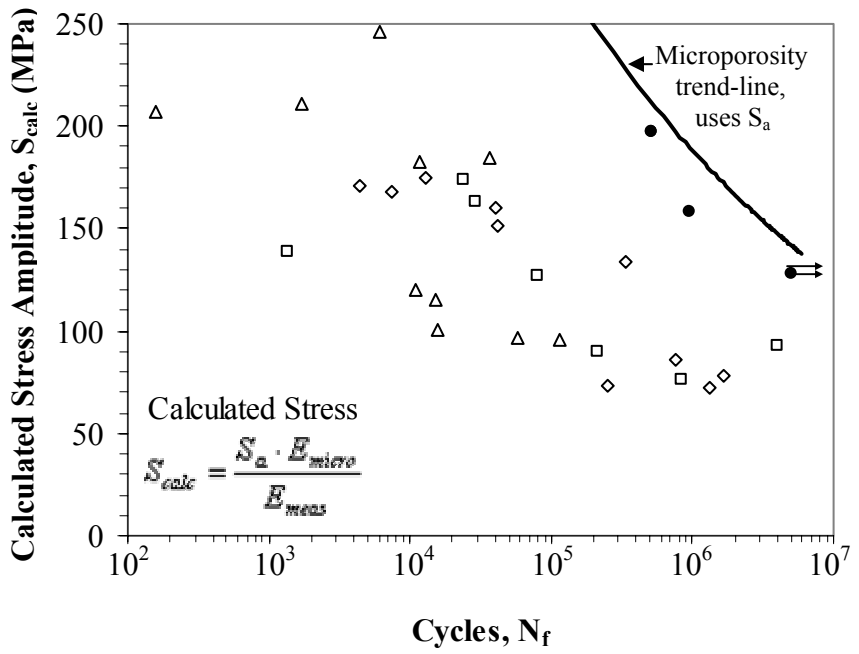

Figure 10 - Calculated stress amplitude macroporosity data; (□) "least" porosity, (◇) "middle" porosity, (△) "most" porosity; and test stress amplitude data S_a for (●) microporosity material

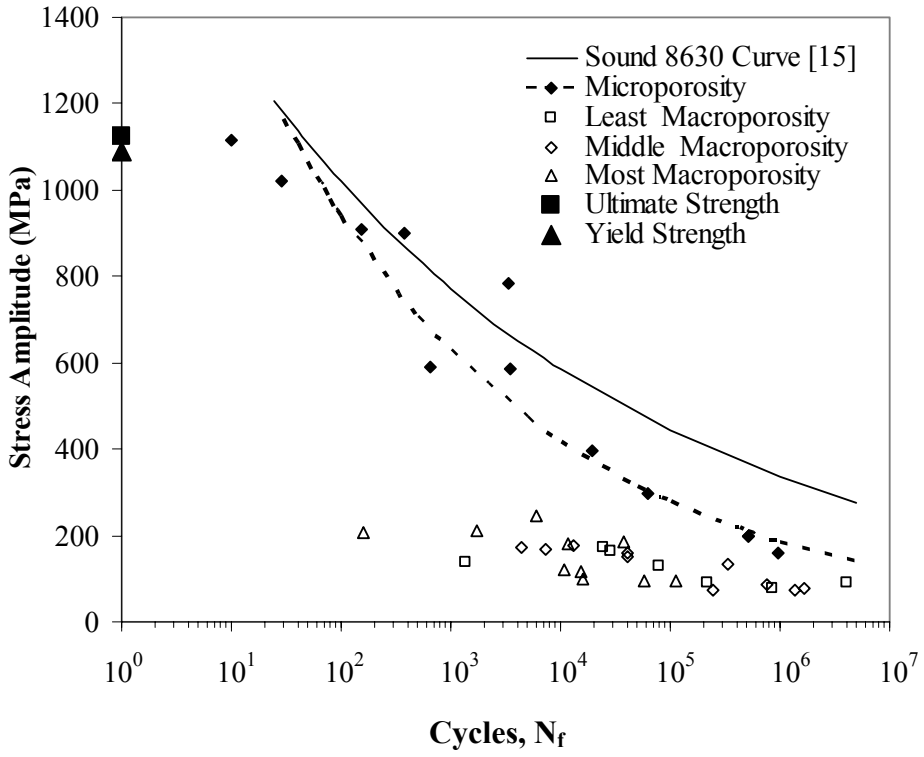

Figure 11 - Stress amplitude versus cycles to failure for sound cast 8630 material property curve[15], microporosity data and macroporosity data using calculated stress amplitude from Equation (3)

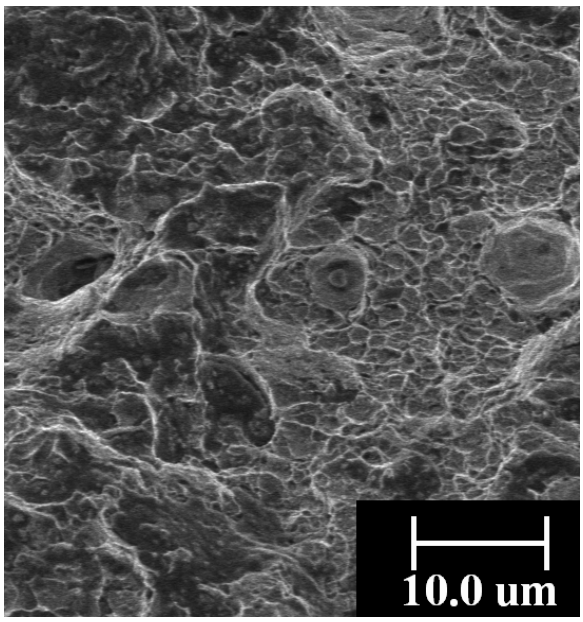

Figure 12 - Typical ductile dimples found in the final fracture regions of microporosity specimen

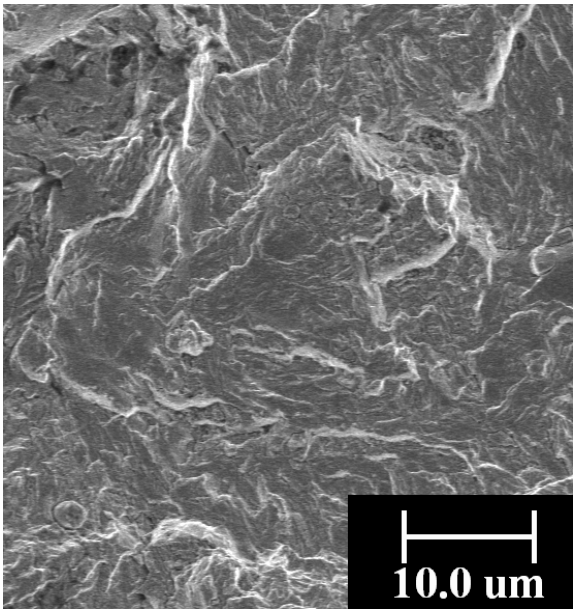

Figure 13 - Typical fatigue facets found in FCG regions

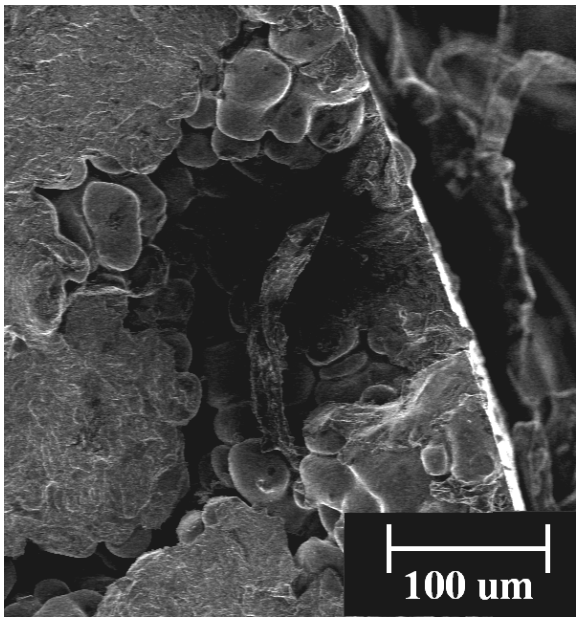

Figure 14 - Near surface micropore of approximately 200 μm diameter

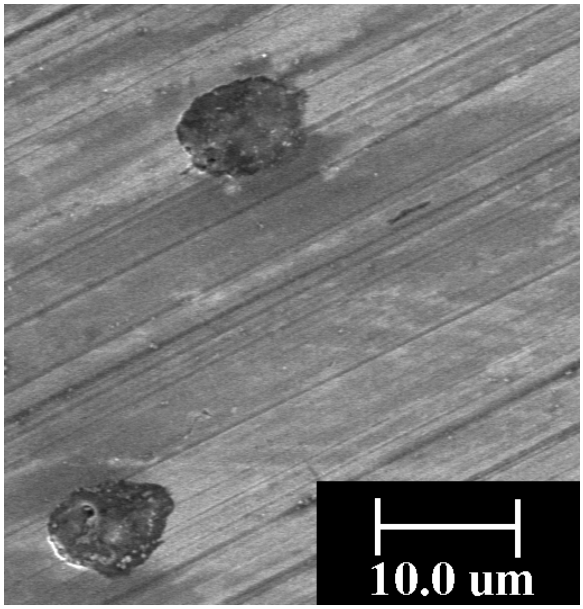

Figure 15 - Typical micropores found on the ground surface

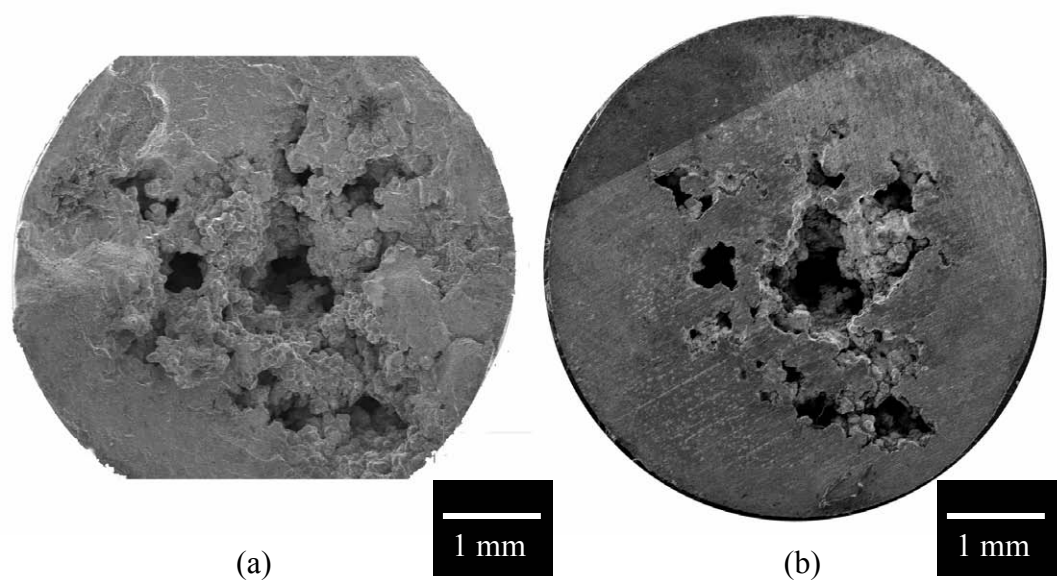

Figure 16 - Macroporosity specimen (a) fracture surface showing signs of FCG near the edges of the specimen and (b) ground surface

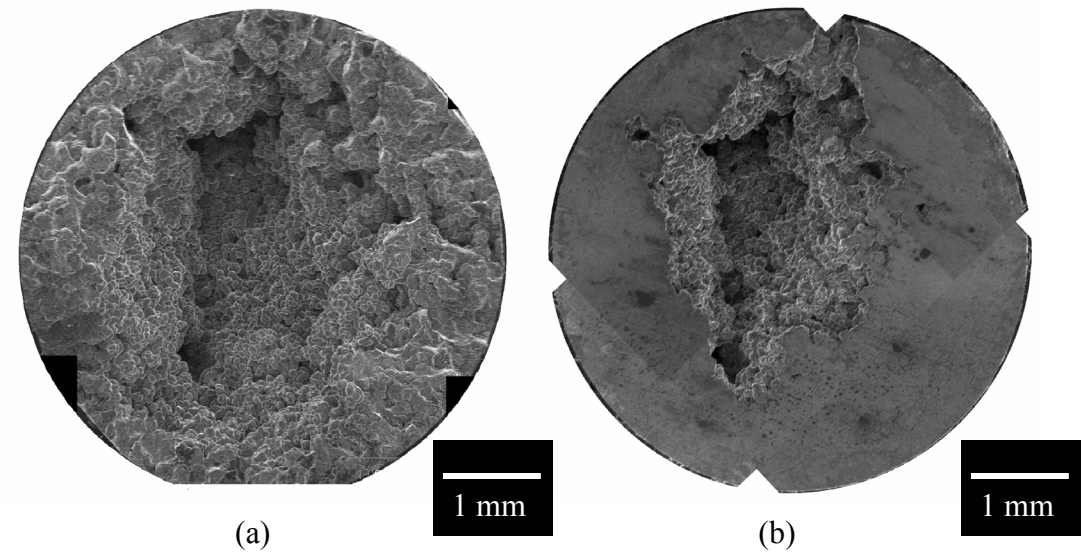

Figure 17 - Macroporosity specimen (a) fracture surface with no signs of macroscopic fracture and (b) ground surface

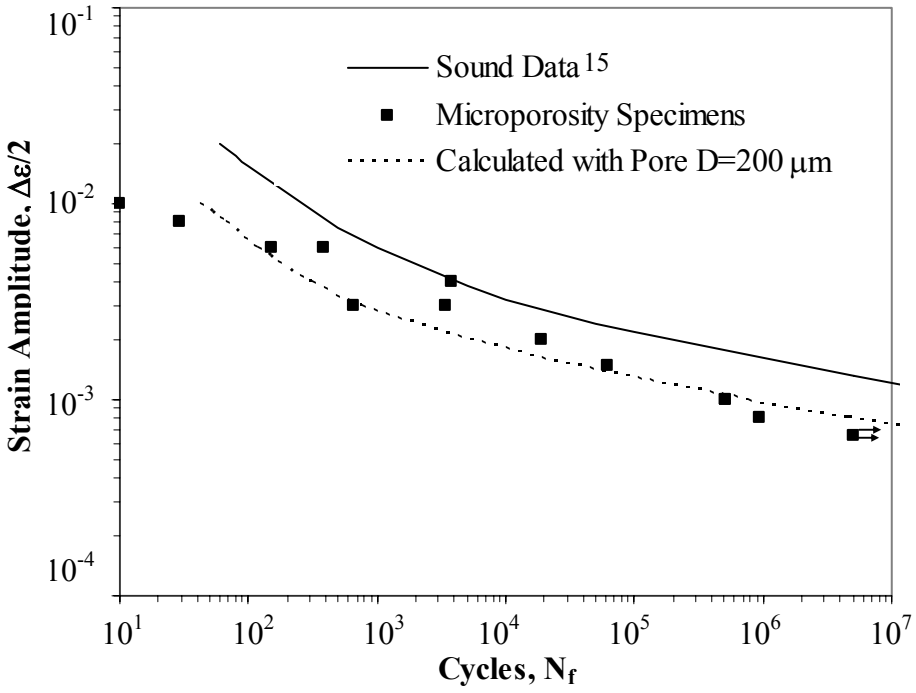

Figure 18 - Local strain-life model calculations for microporosity specimens assuming a 200 μm diameter surface notch

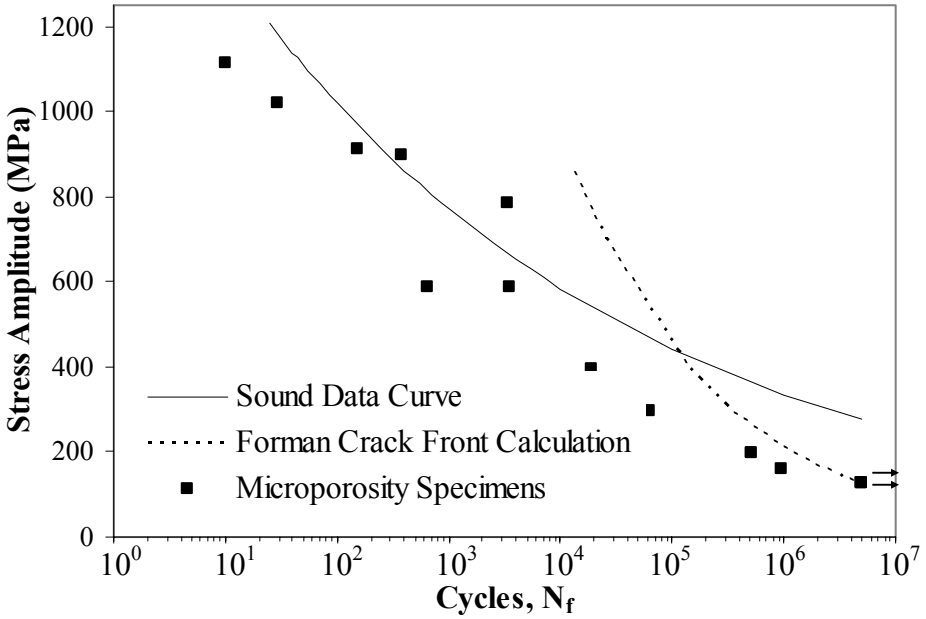

Figure 19 - LEFM model calculations for microporosity specimens using a crack length based on a 200 μm pore

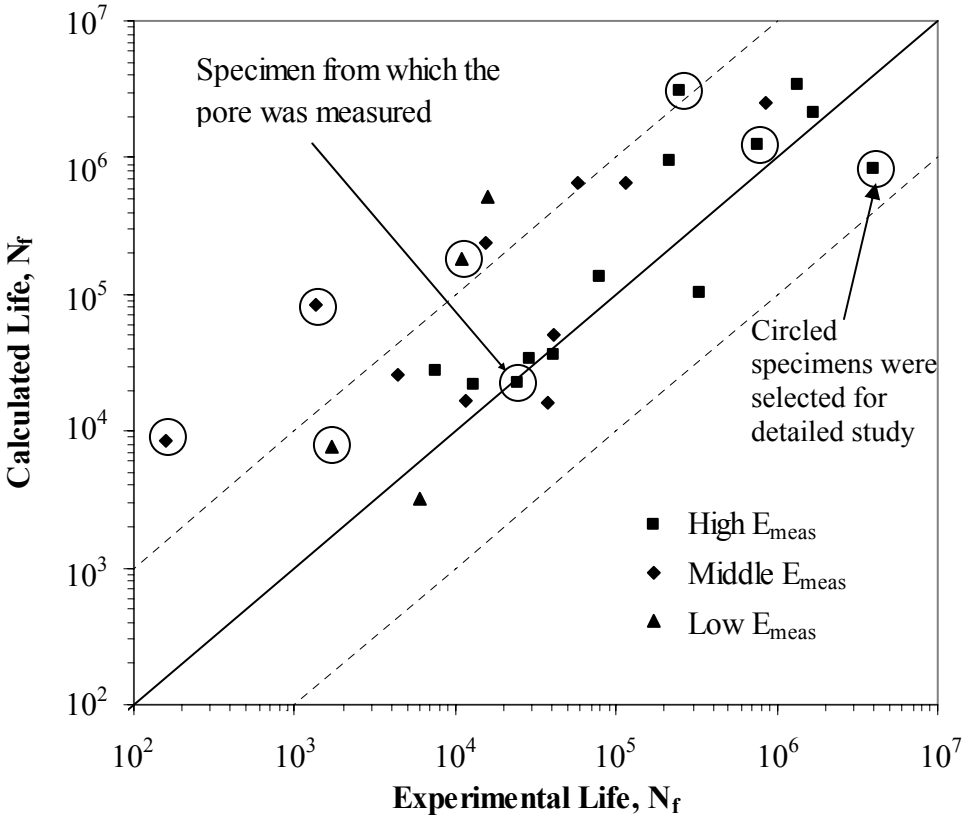

Figure 20 - Calculated vs. experimental life for strain-life modeling based on typical macropore sphere found in specimen C4, R_{pore} = 0.75 mm

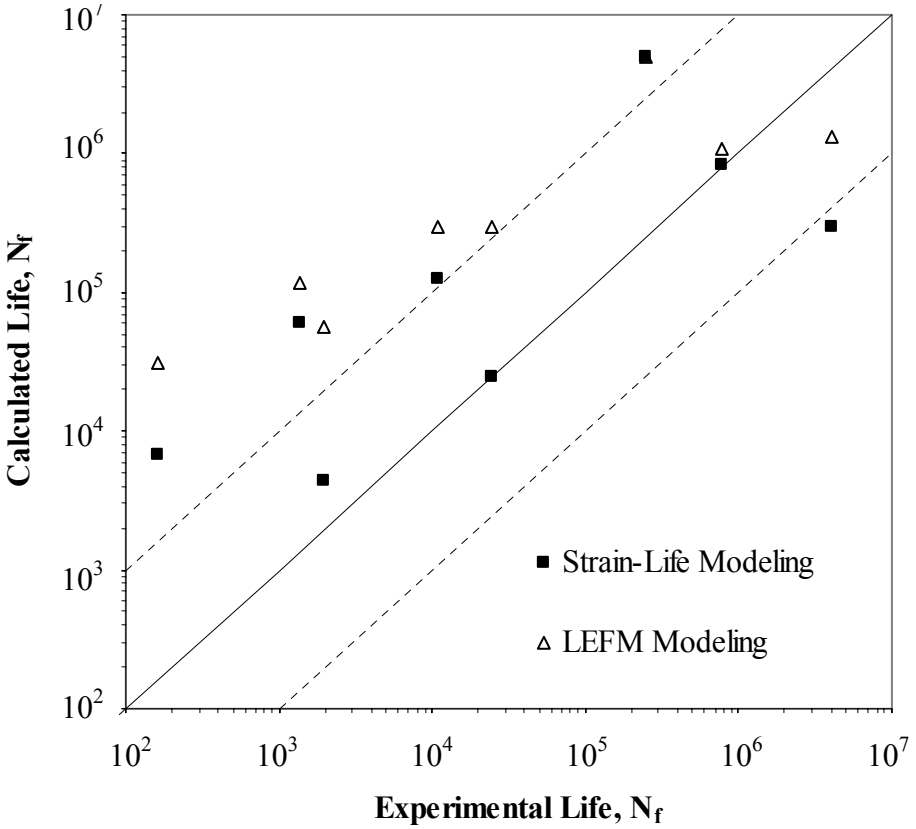

Figure 21 - Calculated vs. experimental life for strain-life and LEFM modeling for the eight identified points in Figure 20 using pore measurements given in Table 4.